Physics Letters B 790 (2019) 237–242

Contents lists available at ScienceDirect

Physics Letters B

www.elsevier.com/locate/physletb

Improved astrophysical rate for the $^{18}O(p,\alpha)^{15}N$ reaction by underground measurements

C.G. Bruno [a,*], M. Aliotta [a,*], P. Descouvemont [b], A. Best [c], T. Davinson [a], D. Bemmerer [d], A. Boeltzig [e,f,1], C. Broggini [g], A. Caciolli [h], F. Cavanna [i], T. Chillery [a], G.F. Ciani [e], P. Corvisiero [i,j], R. Depalo [h], A. Di Leva [c], Z. Elekes [k], F. Ferraro [i,j], A. Formicola [f], Zs. Fülöp [k], G. Gervino [l], A. Guglielmetti [m], C. Gustavino [n], Gy. Gyürky [k], G. Imbriani [c], M. Junker [f], M. Lugaro [o], P. Marigo [g,h], R. Menegazzo [h], V. Mossa [p], F.R. Pantaleo [p], D. Piatti [h], P. Prati [i,j], K. Stöckel [d,q], O. Straniero [f,r], F. Strieder [s], T. Szücs [d,k], M.P. Takács [d,q], D. Trezzi [m]

[a] SUPA, School of Physics and Astronomy, University of Edinburgh, EH9 3FD Edinburgh, United Kingdom
[b] Physique Nucléaire Théorique et Physique Mathématique, C.P. 229, Université Libre de Bruxelles (ULB), B 1050 Brussels, Belgium
[c] Università di Napoli "Federico II", and INFN, Sezione di Napoli, 80126 Napoli, Italy
[d] Helmholtz-Zentrum Dresden-Rossendorf, Bautzner Landstr. 400, 01328 Dresden, Germany
[e] Gran Sasso Science Institute, Viale F. Crispi 7, 67100 L'Aquila, Italy
[f] INFN, Laboratori Nazionali del Gran Sasso (LNGS), 67100 Assergi, Italy
[g] INFN, Sezione di Padova, Via F. Marzolo 8, 35131 Padova, Italy
[h] Università degli Studi di Padova and INFN, Sezione di Padova, Via F. Marzolo 8, 35131 Padova, Italy
[i] INFN, Sezione di Genova, Via Dodecaneso 33, 16146 Genova, Italy
[j] Università degli Studi di Genova, Via Dodecaneso 33, 16146 Genova, Italy
[k] Institute for Nuclear Research (MTA ATOMKI), PO Box 51, HU-4001 Debrecen, Hungary
[l] Università degli Studi di Torino and INFN, Sezione di Torino, Via P. Giuria 1, 10125 Torino, Italy
[m] Università degli Studi di Milano and INFN, Sezione di Milano, Via G. Celoria 16, 20133 Milano, Italy
[n] INFN, Sezione di Roma, Piazzale A. Moro 2, 00185 Roma, Italy
[o] Konkoly Observatory, Research Centre for Astronomy and Earth Sciences, Hungarian Academy of Sciences, 1121 Budapest, Hungary
[p] Università degli Studi di Bari and INFN, Sezione di Bari, 70125 Bari, Italy
[q] Technische Universität Dresden, Institut für Kern- und Teilchenphysik, Zellescher Weg 19, 01069 Dresden, Germany
[r] Osservatorio Astronomico di Collurania, Teramo, and INFN, Sezione di Napoli, 80126 Napoli, Italy
[s] South Dakota School of Mines & Technology, 501 E. Saint Joseph St., SD 57701, USA

ARTICLE INFO

Article history:
Received 23 November 2018
Received in revised form 9 January 2019
Accepted 11 January 2019
Available online 17 January 2019
Editor: W. Haxton

Keywords:
Stellar hydrogen burning
Hydrostatic stellar nucleosynthesis

ABSTRACT

The $^{18}O(p,\alpha)^{15}N$ reaction affects the synthesis of ^{15}N, ^{18}O and ^{19}F isotopes, whose abundances can be used to probe the nucleosynthesis and mixing processes occurring deep inside asymptotic giant branch (AGB) stars. We performed a low-background direct measurement of the $^{18}O(p,\alpha)^{15}N$ reaction cross-section at the Laboratory for Underground Nuclear Astrophysics (LUNA) from center of mass energy $E_{c.m.} = 340$ keV down to $E_{c.m.} = 55$ keV, the lowest energy measured to date corresponding to a cross-section of less than 1 picobarn/sr. The strength of a key resonance at center of mass energy $E_r = 90$ keV was found to be a factor of 10 higher than previously reported. A multi-channel R-matrix analysis of our and other data available in the literature was performed. Over a wide temperature range, $T = 0.01$–1.00 GK, our new astrophysical rate is both more accurate and precise than recent evaluations. Stronger constraints can now be placed on the physical processes controlling nucleosynthesis in AGB stars with interesting consequences on the abundance of ^{18}O in these stars and in stardust grains, specifically on the production sites of oxygen-rich Group II grains.

© 2019 The Author(s). Published by Elsevier B.V. This is an open access article under the CC BY license (http://creativecommons.org/licenses/by/4.0/). Funded by SCOAP[3].

* Corresponding authors.
E-mail addresses: carlo.bruno@ed.ac.uk (C.G. Bruno), m.aliotta@ed.ac.uk (M. Aliotta).
[1] Current address: University of Notre Dame, Department of Physics, 225 Nieuwland Science Hall, Notre Dame, IN 46556, USA.

https://doi.org/10.1016/j.physletb.2019.01.017
0370-2693/© 2019 The Author(s). Published by Elsevier B.V. This is an open access article under the CC BY license (http://creativecommons.org/licenses/by/4.0/). Funded by SCOAP[3].

1. Introduction

The ^{18}O(p,α)^{15}N reaction influences the abundances of ^{15}N, ^{18}O and ^{19}F isotopes [1,2], critical to constrain a wide variety of stellar models. For example, the O isotopic ratios observed in asymptotic giant branch (AGB) stars of different masses [3–5] can be used to probe the nucleosynthesis and mixing processes in these stars. Furthermore, the ^{18}O/^{16}O abundance ratio is critical in classifying stardust oxide and silicate grains that originally condensed in AGB stars, supernovae, and novae and can be found preserved in meteorites [6,7]. One striking example is given by oxygen-rich Group II grains whose experimentally measured ^{18}O/^{16}O ratios are significantly higher than predicted by models, and dilution with matter of solar composition is currently assumed to explain this discrepancy (*e.g.*, [8]). A low-background measurement of the ^{18}O(p,α)^{15}N reaction at energies of astrophysical interest can result in more accurate predictions for the O isotopic composition and place stronger constraints on the stellar sites from where these grains originate [8,9].

The ^{18}O(p,α)^{15}N reaction (Q-value = 3.98 MeV) has been studied using both direct [10–12] and indirect [13,14] approaches. At temperatures of astrophysical interest (T = 0.01–1.00 GK), its rate is dominated by the interference of three $J^\pi = 1/2^+$ resonances at center of mass energies E_r = 143, 610 and 800 keV, respectively. For the latter two resonances, results on their energy and partial widths are largely inconsistent [14], and tensions have also been reported between the cross section of different datasets at energies $E_{\rm c.m.} \leq 1$ MeV [14]. While the excitation function has been measured directly to energies as low as $E_{\rm c.m.} = 70$ keV [11], significant uncertainties remain that affect the cross-section extrapolation to lower energies. In addition, the energy and partial widths of a $E_r = 90$ keV resonance were questioned in recent theoretical work [15]. As a consequence, the stellar reaction rate still contains significant uncertainties.

This letter presents the results of a direct underground measurement of the ^{18}O(p,α)^{15}N reaction cross-section from $E_{\rm c.m.}$ = 340 keV down to $E_{\rm c.m.} = 55$ keV, the lowest energy measured to date. The primary aim of the present study was to measure the non-resonant component of the cross section of the ^{18}O(p,α)^{15}N reaction at proton beam energies from $E_p = 360$ to 60 keV, extending the range of direct measurements to energies of interest for intermediate and low-mass AGB stars. We also aimed to determine, with improved accuracy, the strength of three resonances of astrophysical interest at $E_{\rm r} = 90$, 200, 320 keV, using the thick-target yield approach, in addition to the $E_{\rm r} = 143$ keV resonance strength already reported [24]. The experiment was performed at the underground LUNA-400 accelerator [16,17] of the Laboratori Nazionali del Gran Sasso (LNGS), Italy, within a program of reaction studies of hydrogen burning in advanced CNO cycles [18–23]. The reduced background achieved underground [24] allowed us to measure cross-sections as low as 1 picobarn/sr with unprecedented precision.

2. Methodology

Full details on the experimental setup are reported in Ref. [24]. Briefly, a proton beam was accelerated onto solid Ta_2O_5 targets enriched (98%) in ^{18}O [26]. Targets were produced with thicknesses corresponding to energy losses of 5 or 15 keV at proton beam energy $E_p = 151$ keV for cross-section measurements respectively above and below $E_p = 103$ keV. Alpha particles from the ^{18}O(p,α)^{15}N reaction were detected at backward angles using an array of eight silicon detectors: four placed at 135° with respect to the beam axis and four at 102.5° (of these, only two were working properly during data taking) [24]. Protective aluminized Mylar foils were mounted in front of each detector. Their thickness (5.5 µm) was chosen so as to stop elastically scattered protons while at the same time letting the alpha particles pass through with minimal energy loss ($\approx$ 800 keV). Typical detection energies were about $E_\alpha = 2.3$ MeV, depending on the proton beam energy.

For narrow and isolated resonances (as those investigated in this study), the resonance strength $\omega\gamma$ can be directly obtained from the thick-target yield Y as [27]:

$$\omega\gamma = \frac{2}{\lambda^2}\epsilon_{\rm eff}\frac{Y}{W\eta} \quad (1)$$

where $\epsilon_{\rm eff}$ is the effective stopping power in units of eV/(atom/cm^2); η is the detection efficiency; λ is the de Broglie wavelength of the projectile at the resonant energy; and W takes into account the angular distribution at the angle of the detector. The W factor (at most 20% deviation from unity in this study) was calculated using an R-matrix approach (see later) based on J^π values reported in previous experimental studies [11,13].

At each beam energy, counts in the alpha peak were obtained by integration [24]. The natural background ($\approx$ 0.04 counts/h/detector) under the alpha peak of the ^{18}O(p,α)^{15}N reaction ($\sim$ 2 MeV) was negligible at all beam energies as a result of the ten-fold background reduction achieved underground at these energies [24]. The only source of background was from beam-induced reactions on trace boron contaminants in the target giving rise to a broad feature around 3 MeV through the ^{11}B(p,α)2α reaction. Its contribution to the ^{18}O(p,α)^{15}N alpha peak was estimated using a linear extrapolation and found to be less than 2% at all energies investigated here. We conservatively assigned an asymmetric uncertainty of −3% to the number of counts in the alpha peak.

3. Results

3.1. Narrow resonances

For the $E_r = 200$ and 320 keV (Fig. 1 top panel) resonances we first determined the non-resonant yield contribution from a second-order polynomial fit of the data points above and below the resonance region, and then added the polynomial function to a fit of the thick-target resonance profile [24]:

$$f(E_{\rm p}) = \frac{H}{\left[1+\exp\left(\frac{E_{\rm R}-E}{\delta_{\rm L}}\right)\right]\left[1+\exp\left(\frac{E-E_{\rm R}-\Delta E}{\delta_{\rm R}}\right)\right]} \quad (2)$$

where H is the plateau height; $E_{\rm R}$ is the resonance energy in the laboratory system; $\delta_{\rm L}$ and $\delta_{\rm R}$ describe, respectively, the steepness of rising and falling edges of the profile; and ΔE is the energy-equivalent target thickness (in the laboratory). This procedure allowed us to extract the net yield $Y(=H)$ used to calculate the resonance strength according to Eq. (1).

The situation was more complicated for the $E_r = 90$ keV resonance (Fig. 1 bottom panel) because data were acquired on 5 keV-thick targets for beam energies $E_{\rm p} > 103$ keV and on 15 keV-thick targets for beam energies $E_{\rm p} \leq 103$ keV to increase the counting rate. Non-resonant yield data taken with both targets were first converted into cross-section data and these latter were fit with a single R-matrix calculation [28]. The fitted cross section was then converted back into a yield curve in order to establish the non-resonant yield contribution (dashed line in Fig. 1) to the thick-target resonance yield. A fit to the thick-target yield plateau (solid line in Fig. 1) was finally performed to extract the resonance strength value. Note that all fits to thick-target yield profiles were performed only on data acquired at 135° to minimize systematic uncertainties in efficiency due to two non-working detectors at 102.5° (see [24] for details).

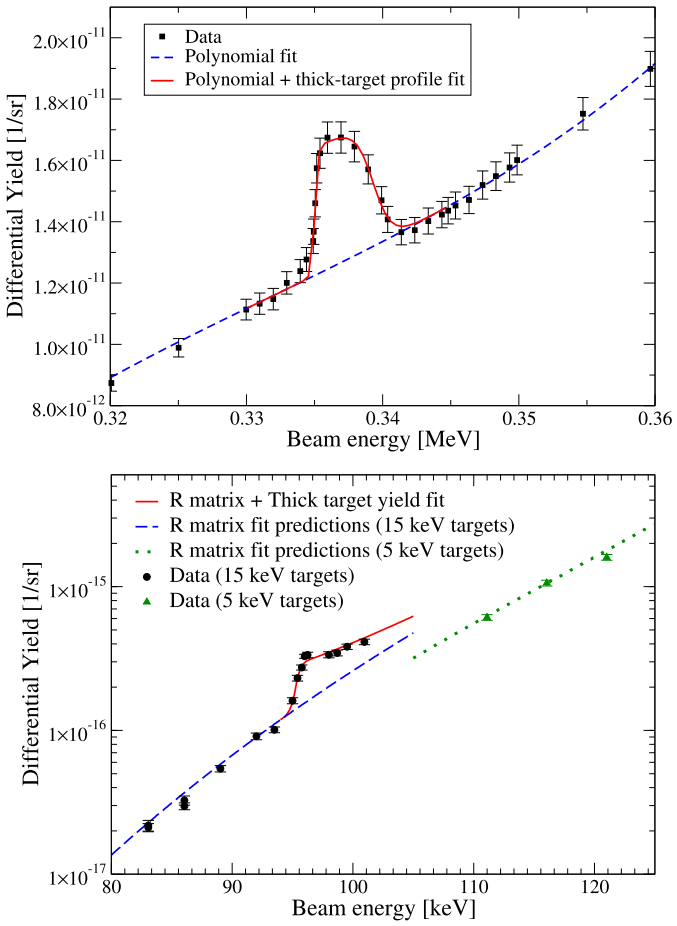

Fig. 1. Thick-target yield profile of the $E_r = 320$ keV (top) and 90 keV (bottom) resonances in the ^{18}O(p,α)^{15}N reaction. The resonance strength was obtained from a fit (red curves) to the yield profile (Eq. (2)) taking into account non-resonant contributions (dashed lines) determined either from a polynomial fit (dashed line, top panel) or from an R-matrix calculation (dashed lines, bottom panel). Error bars show statistical uncertainties (see Table 2). The differential yield shown on the ordinate is defined here as the yield divided by the solid angle.

Table 1
Resonance energies and strengths $\omega\gamma$ for the three resonances in ^{18}O(p,α)^{15}N measured in this work and previously. The uncertainty on the resonant energies of this work corresponds to our beam energy resolution [29]. Statistical (st) and systematic (sy) uncertainties are reported for this work. Other works report total uncertainties only.

E_r [keV]	$\omega\gamma$ [meV]	Ref.
90 ± 3	$(0.16 \pm 0.05) \times 10^{-3}$	[11]
96.6 ± 2.2	$(0.18 \pm 0.03) \times 10^{-3}$	[13]
90.3 ± 0.3	$(1.57 \pm 0.14_{st} \pm 0.12_{sy}) \times 10^{-3}$	this work
143.9 ± 0.9	170 ± 20	[11]
142.8 ± 0.1	167 ± 12	[30]
143.2 ± 0.3	$164.2 \pm 0.9_{st} \pm^{+12.1}_{-11.7}{}_{sy}$	[24]
205 ± 1	2.3 ± 0.6	[11]
204.7 ± 0.3	$2.37 \pm 0.12_{st} \pm 0.18_{sy}$	this work
316 ± 1	57 ± 10	[11]
317.0 ± 0.3	$85 \pm 9_{st} \pm 7_{sy}$	this work

Resonance strengths obtained in the present study for all three resonances, as well as for the $E_r = 143$ keV resonance already reported in Ref. [24], are shown in Table 1, with uncertainties given in Table 2. The $\omega\gamma$ values for the $E_r = 200$ and 320 keV resonances are in fair agreement with previous determinations while the strength of the $E_r = 90$ keV resonance is an order of magnitude higher than previously reported in Lorenz-Wirzba et al. [11] and La Cognata et al. [13]. We note however that in her PhD thesis [32], Lorenz-Wirzba reports $\omega\gamma = 2.1 \pm 0.6$ μeV in excellent agreement with our present value. It is unclear why different values for this strength appear in Refs. [11,32] but the discrepancy is likely due to an over-estimate of the poorly-known total width Γ_{tot} of this $E_r = 90$ keV resonance in Ref. [11]. In our study we have sufficient data to fit the yield (Fig. 1), and we do not need to assume a Γ_{tot} value to determine a resonance strength.

Table 2
Error budget for statistical (tail asymmetry, background subtraction, charge integration) and systematic (stopping power, efficiency) uncertainties.

Source	Rel. uncertainty	Ref.
Tail asymmetry	+2.0%	[24]
Background subtraction	−3.0%	this work
Charge integration	±2.0%	[24]
Stopping power	±4.0%	[31]
Efficiency	±5.5%	[24]

Table 3
Data sets included in our global R-matrix fit.

Reaction	$E_{c.m}$ [keV]	θ_{lab} [°]	Reference
^{18}O(p,α)^{15}N	55–320	102.5, 135	this work
^{18}O(p,α)^{15}N	220–660	integrated	[10]
^{18}O(p,α)^{15}N	70–886	90, 135	[11]
^{18}O(p,α)^{15}N	590–1670	several	[12]
^{18}O(p,p)^{18}O	570–1340	90, 140	[36]

3.2. *R-matrix analysis*

The differential cross-section was calculated from our differential yield data points using the median energy approach described in Ref. [33]. More details on this deconvolution analysis can be found in Ref. [34]. Electron screening corrections (at most 20% here) based on the adiabatic limit approximation [35] were applied to each cross-section data point.

To arrive at a final reaction rate, we performed a global multichannel R-matrix [28] analysis on our differential cross-sections, at both 135° and 102.5°, and the most recent ^{18}O(p,α)^{15}N and ^{18}O(p,p)^{18}O datasets (Table 3). The inclusion of elastic-scattering data in the fitting procedure provides strong constraints on the R-matrix fits since the pole energies and proton widths are identical. However, for the additional datasets considered here we had to rely on digitized information from the EXFOR database [37] because original data were not available. Similarly, error bars were either unavailable or unreliable (if obtained from the digitization procedure, *e.g.* for errors smaller than the symbol size). Therefore, the statistical uncertainty on all data points was arbitrarily set to ±10% unless the digitized uncertainty (where available) was higher. Statistical uncertainties in our cross-section data points were calculated as a combination in quadrature of Poisson uncertainty, tail asymmetry and background subtraction (see Table 2). Furthermore, the 0.3 keV uncertainty in the energy of each data point of this work was converted into an uncertainty in the corresponding cross-section and added in quadrature to the other statistical uncertainties.

Our global R-matrix fit is shown in Fig. 2 with our data and those from Ref. [11] (top panel) in the form of the (differential)

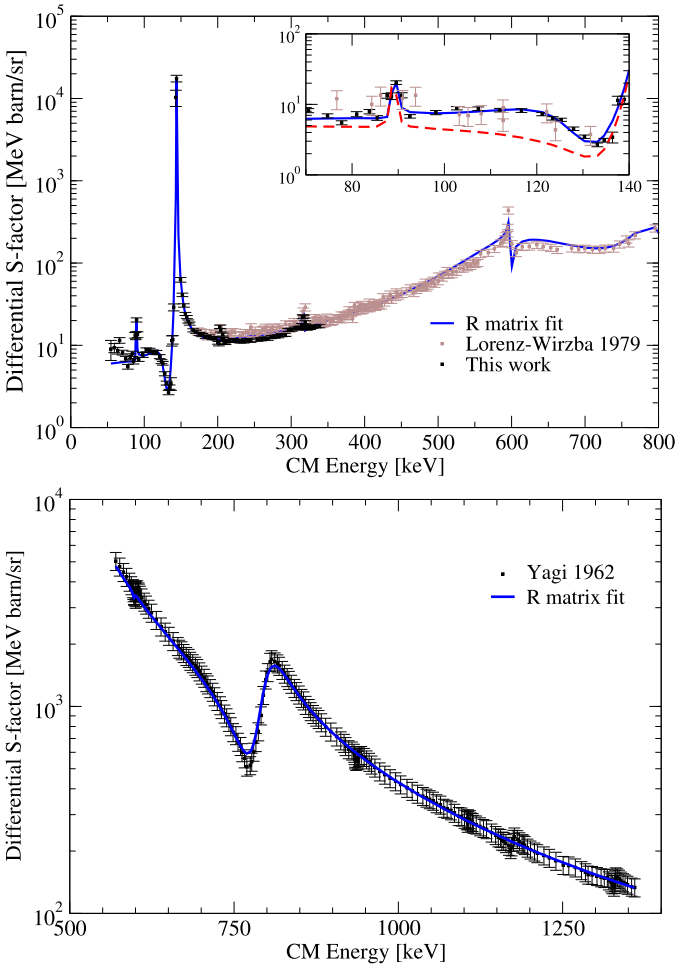

Fig. 2. Global R-matrix fit (solid line) shown together with ^{18}O(p,α)^{15}N differential S-factor data at 135° from our study and from Ref. [11] (top panel); and with ^{18}O(p,p)^{18}O elastic scattering data at 140° from [36] (bottom panel). The red dashed lined in the inset shows the effect of removing the new state at $E_r = 106$ keV.

astrophysical $S(E)$ factor,[2] and with elastic scattering data from Ref. [36] (bottom panel).

Some tensions between our data and those reported in Ref. [11] at resonant energies below $E_{\text{c.m.}} = 170$ keV (Fig. 2 top panel, inset) may be the result of an incorrect (in the sense of Ref. [33]) deconvolution of the median energy near the strong $E_r = 143$ and 90 keV resonances. This deconvolution is less problematic at higher, non-resonant energies. The tensions observed at resonant energies could be resolved by increasing the uncertainties in data from [11], but this strategy would result in a lower reduced chi-square $\tilde{\chi}^2$ value without any added physics constraints to the data. Instead, we decided to discard data from [11] below $E_{\text{c.m.}} = 170$ keV for both angles (approximately 10% of the data set).

R-matrix fits were carried out using both AZURE2 [38] and rmatrix2015 [39] independently. The R-matrix radius was set to $a = 5\,\text{fm} \simeq 1.4\,\text{fm} \times (18^{1/3} + 1^{1/3})$, but we observed no significant differences using $a = 5.5$ or 6 fm. We used a proton (alpha) separation threshold value of $S_p = 7993.599(1)$ keV ($S_\alpha = 4013.799(1)$ keV) [40]. Angular distribution values were taken from [11], except for the $E_r = 90$ keV resonance for which we used more recent information in [13] instead. In addition, a background pole [28] was also included. However, even by adding a background pole and by optimizing interference effects between resonances, we were unable to reproduce the broad structure observed around $E_{\text{c.m.}} = 110$ keV (Fig. 2), unless by assuming the existence of a hitherto unobserved new resonance at $E_r = 106$ keV. This new resonance is not incompatible with previous data from Lorenz-Wirzba et al. [11] at 135° (Fig. 2). Because of our limited angular information (detectors were placed at two angles only), we were only able to tentatively assign a spin-parity of $J^\pi = 1/2^-$ to this new state based on the lowest $\tilde{\chi}^2$ value obtained from the R-matrix fit (see below).

Table 4
R-matrix best-fit parameters values (center-of-mass): in bold-face, values obtained from fits to thick-target yields (Table 1) and included in the calculation, but not optimized by the fit. Note the inclusion of a previously unobserved resonance at $E_r = 106$ keV with tentative spin-parity assignments in brackets, and the presence of a background pole at 7 MeV. Uncertainties (from MINUIT) are statistical only. The last column gives the off-diagonal interference sign between resonances.

J^π	E_r [keV]	Γ_p	Γ_α	Int.
$1/2^+$	**142.8 ± 0.3**	**164 ± 12 meV**	150 ± 1 eV	+
$1/2^+$	612.5 ± 1.2	7.7 ± 0.1 keV	163 ± 1 keV	−
$1/2^+$	799.8 ± 0.3	24.4 ± 0.3 keV	26.1 ± 0.3 keV	+
$3/2^-$	597.6 ± 0.3	36 ± 2 eV	2.5 ± 0.1 keV	+
$3/2^+$	89.0 ± 0.3	**797 ± 57 neV**	121 ± 5 eV	+
$5/2^+$	**204.7 ± 0.3**	**791 ± 56 μeV**	12 ± 1 eV	+
$5/2^+$	**317.2 ± 0.3**	**28.2 ± 2.0 meV**	1.9 ± 0.1 keV	−
$(1/2^-)$	106 ± 3	120 ± 10 μeV	86 ± 1.6 keV	+
$1/2^-$	**7000**	29 ± 12 MeV	431 ± 180 MeV	+

R-matrix results with AZURE2 and rmatrix2015 were in excellent agreement. However, AZURE2 offers the possibility of defining scaling factors for each dataset that can be treated as additional degrees of freedom and optimized during the fitting procedure [38]. These scaling factors can help attenuate systematic tensions between datasets and effectively model their systematic uncertainty. We arbitrarily set all scaling factors to a value of ±7%, corresponding to the total percent systematic uncertainty in our data. Using AZURE2 with a proper normalization coefficient and increased uncertainties as discussed above, we minimized the $\tilde{\chi}^2$ using the MINUIT package included in AZURE2. Best-fit parameters are given in Table 4.

3.3. Reaction rate calculation

Recent ^{18}O(p,α)^{15}N astrophysical reaction rates available in the literature [41,42] were calculated using `RatesMC` [43], which can only simultaneously treat interferences between resonances with the same J^π two at a time. However, since the low energy cross section of the ^{18}O(p,α)^{15}N reaction is determined by the presence of *three* $J^\pi = 1/2^+$ states, rates calculated with `RatesMC` have to combine different calculations with different pairs of interfering resonances, discarding the influence of one resonance in turn in each calculation.

A more accurate result can obtained by fully treating the interference effects of all states simultaneously. To this end, we numerically integrated the total cross section obtained with AZURE2 using the parameters in Table 4 (including the background pole) and adding the $E_r = 20$ keV resonance following Ref. [42]. Our recommended reaction rate, normalized to the Iliadis 2010 rate [41] (calculated with `RatesMC`), is shown in Fig. 3. Uncertainties were calculated by varying the parameters in Table 4 by ±1

[2] The $S(E)$ factor is defined as $S(E) = \sigma(E)\exp(2\pi\eta)E$, where $\sigma(E)$ is the reaction cross section, η is the Sommerfeld parameter, and E is the interaction energy [27].

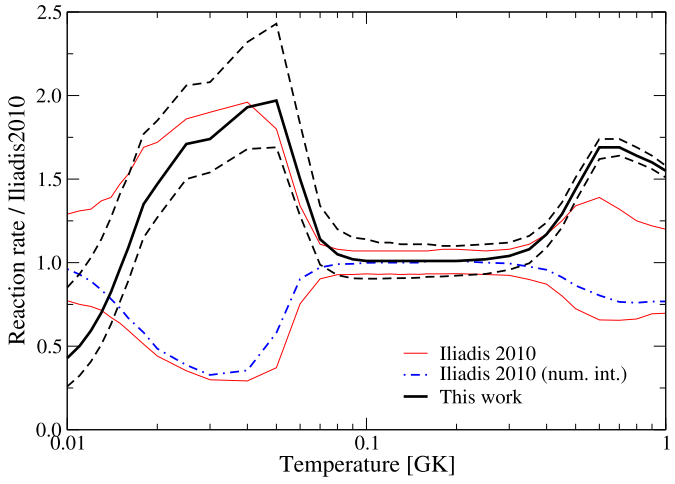

Fig. 3. Reaction rates for the ^{18}O(p,α)^{15}N reaction, calculated by numerical integration of the total cross-section using the parameters in Table 4 of this work (black curve, dashed lines show uncertainties), and Iliadis et al. [41] (blue dashed and dotted line). All curves are normalized to the rate reported in Iliadis et al. [41], calculated with RatesMC. Uncertainties for this latter rate are shown as red lines.

sigma with respect to their central value. To highlight the difference between the two approaches, we also show the rate that would be obtained by numerically integrating the cross sections calculated with AZURE2 using the parameters in Iliadis et al. [41]. This rate (blue dot-dashed line) is also normalized to the Iliadis 2010 (RatesMC) rate in Fig. 3.

Thanks to the extension of the direct data energy range down to $E_{\rm c.m.} = 55$ keV in the present study, and the significant reduction of the uncertainty in the cross-section below $E_{\rm c.m.} = 340$ keV, improved constraints are now available for the calculation of the interference effects between the three $J^\pi = 1/2^+$ resonances. In particular, at temperatures $T < 0.1$ GK, our rate is up to a factor of 2.5 higher than the Iliadis 2010 rate (RatesMC), or about a factor of 5 higher than the numerically integrated rate calculated from the parameters in Iliadis 2010. The uncertainty in our reaction rate is also reduced by up to an order of magnitude over an extended temperature range, $T = 0.01$–1.0 GK.

4. Astrophysical implications

The reported increase of the ^{18}O(p,α)^{15}N reaction rate over a wide temperature range ($T = 0.01$–1.0 GK) has implications in a number of stellar sites. In particular, using our rate, models predict ^{18}O/^{16}O ratios for oxygen-rich Group II grains lower than previously assumed [8], reinforcing the need for dilution with matter of solar composition to explain the discrepancy. Fig. 4 shows the evolution of the ^{18}O and ^{15}N abundances during the Thermally Pulsing Asymptotic Giant Branch (TP-AGB) phase of a star with initial mass $M = 4.8$ M$_\odot$ and solar-like metallicity $Z = 0.014$, that undergoes a mild Hot Bottom Burning (HBB) [44]. Nucleosynthesis calculations are carried out with both the reaction rate presented in this work (right) and in Iliadis 2010 [41] (left). As a result of the new reaction rate, the ^{18}O mass fraction is reduced by an order of magnitude, and with significantly reduced uncertainties, at the end of the evolution due to the operation of HBB compared to the previously adopted rate. This reduction is observed only for stars undergoing mild HBB ($T \simeq 40$–60 MK), corresponding to a narrow stellar mass range around $M \simeq 4.5$–5 M$_\odot$, depending on the stellar evolution code used and the metallicity. Our new rate introduces stars in this narrow mass range as a potential new site for the production of some grains, requiring no dilution with material of Solar System composition. In particular, AGB stellar models [45] of 5 M$_\odot$

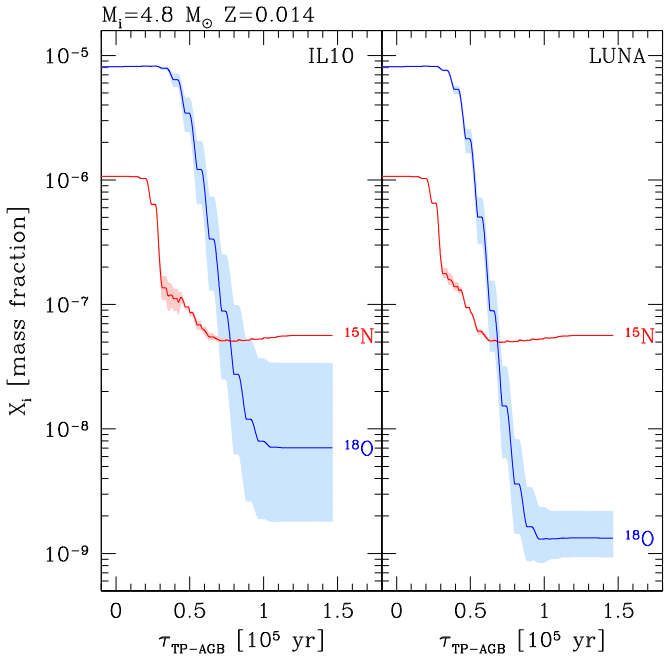

Fig. 4. Evolution of ^{15} N and ^{18}O surface abundances during the entire TP-AGB phase of a star with initial mass of 4.8 $M_\odot$ and solar metallicity $Z = 0.014$, computed with the COLIBRI code [44]. Predictions obtained with the rate from Iliadis 2010 (left) and the new one from LUNA (right) are shown together with the corresponding uncertainty ranges.

and metallicity $Z = 0.03$ could produce grains with ^{18}O/^{16}O down to 5×10^{-4} and ^{17}O/^{16}O $= 1.7 \times 10^{-3}$. These values are very close to those reported in corundum grain T84, an outlying oxygen-rich Group II grain, having ^{18}O/^{16}O $= 4.5 \times 10^{-4}$, ^{17}O/^{16}O $= 1.5 \times 10^{-3}$, without the need to assume dilution with material of solar composition. Data on the aluminum isotopic ratios of this type of grains is needed to confirm this new possible production site. Complete astrophysical implications of CNO rates recently measured at LUNA [18,20,21,25], including the rate presented here, require more in-depth and comprehensive astrophysical analyses that go beyond the scope of this Letter and will be the subject of a forthcoming publication.

5. Conclusions

We reported an improved ^{18}O(p,α)^{15}N reaction measurement extending the reach of direct measurements down to $E_{\rm c.m.} = 55$ keV, the lowest energy to date, with unprecedented precision. Resonance energies and strengths for key astrophysical states are in good agreement with previous work, except for the $E_r = 90$ keV resonance whose strength value of $1.57 \pm 0.14_{\rm stat} \pm 0.12_{\rm syst}$ μeV is an order of magnitude higher than previously reported [11,13]. A multi-channel R-matrix analysis of our new cross-section data and other datasets available in the literature was performed to extrapolate the cross-section to energies of astrophysical interest. The R-matrix fit presented in this work is the first attempt, to our knowledge, at fitting all available datasets, including elastic scattering, to minimize the statistical and systematic uncertainties. Thanks to the improved constraints offered by the new underground measurement, our recommended ^{18}O(p,α)^{15}N reaction rate is more precise than the rate presented in Ref. [41] over a wide temperature range ($T = 0.01$–1.00 GK) of interest in AGB stars. In particular, our results reinforce the need to assume dilution with matter of solar composition to reproduce observed abundances of most oxygen-rich Group II grains originating in intermediate-mass AGB stars [8]. For some outlying oxygen-rich Group II grains, the

present rate suggests a new potential production site requiring no dilution to match experimental isotopic ratios. More data on this type of grains is highly desirable.

The authors acknowledge A.I. Karakas for providing the stellar structure of the 5 $M_{\odot}$ Monash model, and R.J. deBoer for a digitization of data from [11]. This work was supported in part by INFN, STFC UK (grant no. ST/L005824/1), NKFIH (grant no. K120666), HAS Lendület (grant no. LP2014-17), and DFG (grant no. BE 4100/4-1). C.G.B. gratefully acknowledges the support of a SUPA Short-Term Visit Award during his stay in Brussels. P.M. acknowledges the support from the ERC Consolidator Grant funding scheme (project STARKEY, G.A. n. 615604).

References

[1] M. Lugaro, et al., Astrophys. J. 615 (2004) 934.
[2] S. Cristallo, et al., Astron. Astrophys. 540 (2014) A46.
[3] C. Abia, et al., Astron. Astrophys. 599 (2017) A39.
[4] O. Straniero, et al., Astron. Astrophys. 598 (2017) A128.
[5] K. Justtanont, et al., Astron. Astrophys. 578 (2015) A115.
[6] E. Zinner, in: A.M. Davis (Ed.), Treatise on Geochemistry, vol. 1, 2nd ed., Elsevier, 2014, pp. 181–213.
[7] L.P. Nittler, et al., Astrophys. J. 483 (1997) 475.
[8] M. Lugaro, et al., Nat. Astron. 1 (2017) 0027.
[9] S. Palmerini, et al., Astrophys. J. 764 (2013) 128.
[10] H.-B. Mak, et al., Nucl. Phys. A 304 (1978) 210.
[11] H. Lorenz-Wirzba, et al., Nucl. Phys. A 313 (1979) 346.
[12] N.S. Christensen, et al., Nucl. Instrum. Methods Phys. B 51 (1990) 97.
[13] M. La Cognata, et al., Phys. Rev. Lett. 101 (2008) 152501.
[14] M. La Cognata, C. Spitaleri, A.M. Mukhamedzhanov, Astrophys. J. 723 (2010) 1512.
[15] H.T. Fortune, Phys. Rev. C 88 (2013) 015801.
[16] H. Costantini, et al., Rep. Prog. Phys. 72 (2009) 086301.
[17] C. Broggini, D. Bemmerer, A. Caciolli, D. Trezzi, Prog. Part. Nucl. Phys. 98 (2018) 55.
[18] D.A. Scott, et al., Phys. Rev. Lett. 109 (2012) 202501.
[19] A. Di Leva, et al., Phys. Rev. C 89 (2014) 015803.
[20] F. Cavanna, et al., Phys. Rev. Lett. 115 (2015) 252501; F. Cavanna, et al., Phys. Rev. Lett. 120 (2018), 239901(E).
[21] C.G. Bruno, et al., Phys. Rev. Lett. 117 (2016) 142502.
[22] R. Depalo, et al., Phys. Rev. C 94 (2016) 055804.
[23] A. Boeltzig, et al., Eur. Phys. J. A 52 (2016) 75.
[24] C.G. Bruno, et al., Eur. Phys. J. A 51 (2015) 94.
[25] F. Ferraro, et al., Phys. Rev. Lett. 121 (2018) 172701.
[26] A. Caciolli, et al., Eur. Phys. J. A 48 (2012) 144.
[27] C. Iliadis, Nuclear Physics of Stars, 2nd edition, Wiley-VCH, 2015.
[28] P. Descouvemont, D. Baye, Rep. Prog. Phys. 73 (2010) 036301.
[29] A. Formicola, et al., Nucl. Instrum. Methods Phys. A 507 (2003) 609–616.
[30] H.W. Becker, et al., Z. Phys. A 351 (1995) 453.
[31] J. Ziegler, SRIM 2013.00, http://srim.org.
[32] H.-M. Lorenz-Wirzba, PhD thesis, Westfälischen Wilhelms-Universität zu Münster, 1978.
[33] C.R. Brune, D.B. Sayre, Nucl. Instrum. Methods Phys. A 698 (2013) 49–59.
[34] C.G. Bruno, PhD thesis, The University of Edinburgh, 2017.
[35] H.J. Assenbaum, K. Langanke, C. Rolfs, Z. Phys. A 327 (1987) 461.
[36] K. Yagi, J. Phys. Soc. Jpn. 17 (4) (1962) 604.
[37] N. Otuka, et al., Nucl. Data Sheets 120 (2014) 272–276.
[38] R.E. Azuma, et al., Phys. Rev. C 81 (2010) 045805.
[39] D.J. Mountford, et al., Nucl. Instrum. Methods A 767 (2014) 359–363.
[40] M. Wang, et al., CPC 36 (12) (2012) 1603.
[41] C. Iliadis, et al., Nucl. Phys. A 841 (2010) 31–250.
[42] A.L. Sallaska, et al., Astrophys. J. Suppl. Ser. 207 (18) (2013).
[43] R. Longland, et al., Nucl. Phys. A 841 (2010) 1–30.
[44] P. Marigo, et al., Mon. Not. R. Astron. Soc. 434 (2013) 488–526.
[45] A.I. Karakas, M. Lugaro, Astrophys. J. 825 (2016) 1.